Revised manuscript submitted to *Composite Structures* (April 2016)

Influence of porosity on ultrasonic wave velocity, attenuation and interlaminar interface echoes in composite laminates: Finite element simulations and measurements

Yosuke Ishii[a,*], Shiro Biwa[a,†], and Akira Kuraishi[b]

[a] *Department of Aeronautics and Astronautics, Graduate School of Engineering, Kyoto University, Katsura, Nishikyo-ku, Kyoto 615-8540, Japan*
[b] *Aerospace Company, Kawasaki Heavy Industries, Ltd., Kakamigahara, Gifu 504-8710, Japan*

ABSTRACT

The influence of porosity on the ultrasonic wave propagation in unidirectional carbon-fiber-reinforced composite laminates is investigated based on the two-dimensional finite element analysis and measurements. Random distributions of pores with different contents and size are considered in the analysis, together with the effects of viscoelastic plies and interlaminar resin-rich regions. The transient reflection waveforms are calculated from the frequency-domain finite-element solutions by the inverse Fourier transform. As the measures for porosity characterization, the ultrasonic wave velocity, attenuation coefficient, and interlaminar interface echo characteristics are examined for 24-ply unidirectional composite laminates. As a result, the wave velocity decreases with the porosity content in a manner insensitive to the pore size. On the other hand, the attenuation coefficient increases both with the porosity content and with the pore size. The time-frequency analysis of the reflection waveforms shows that the temporal decay rate of interlaminar interface echoes at the stop-band frequency is a good indicator of the porosity content. The measured porosity-content dependence of the wave velocity is better reproduced by the numerical simulations when the interlayer interfacial stiffnesses are adjusted according to the porosity content, indicating that not only the porosity features but also the interlaminar interfacial properties vary with curing conditions.

Keywords: Carbon fiber reinforced plastics; Porosity; Ultrasonic wave; Finite element analysis; Nondestructive evaluation

[*] Presently affiliated with the Department of Mechanical Engineering, Toyohashi University of Technology, Hibarigaoka, Tempaku-cho, Toyohashi 441-8580, Japan.
[†]Corresponding author: Tel.: +81 75 383 3796.
E-mail address: biwa@kuaero.kyoto-u.ac.jp.

1. Introduction

Wide applications of carbon-fiber-reinforced plastics (CFRP) in aerospace, automotive, civil, and marine industries have considerably increased the importance of nondestructive evaluation for their diagnosis. It is recognized that one of the detrimental defects in CFRP laminates is the porosity [1], i.e., distribution of minute pores within the laminate. Porosity levels of more than 2 % by volume fraction [2] can significantly degrade the mechanical properties of the composite laminates such as interlaminar shear strength [3–7], flexural strength [3,8], tensile strength [4,7], compression strength [9], etc. For this reason, the nondestructive evaluation of the porosity content is essential and has been the subject of extensive investigation.

Conventional techniques to evaluate the porosity content have been based on the ultrasonic wave velocity [10–15] and attenuation [15–27] in the stacking direction of composite laminates. In practice, the attenuation is used more frequently than the wave velocity because of its higher sensitivity to the porosity content [2]. In particular, the slope of the attenuation coefficient with respect to the frequency has been shown to be useful for the estimation of porosity content [5, 18]. More recently, the interlaminar interface echoes, also called structural [28] or backscattered signals [29, 30], have been studied as an alternative parameter to evaluate the porosity content.

In order to corroborate the experimental findings for nondestructive porosity characterization, the numerical simulation of ultrasonic wave propagation is particularly effective as it can model the content, size, and arrangement of pores in the composite in a controlled manner. Finite difference [26–28] as well as finite element methods [31] have been adopted to simulate the ultrasonic wave propagation in porosity-containing composite materials. In these previous works, the composites are modeled as elastic solids with distributed pores. In polymer-based composite materials, however, the viscoelastic nature of plies has a significant effect on the wave attenuation. Furthermore, the interlaminar resin-rich zones can also affect the wave propagation behavior. These features should be accounted for in an appropriate manner when the effect of porosity on the wave propagation characteristics in composite laminates is to be evaluated by computational modeling.

In this paper, the two-dimensional finite element simulations of ultrasonic wave

propagation in porosity-containing unidirectional CFRP laminates are presented. In contrast to the aforementioned works [26–28, 31], the present analysis is carried out in the frequency domain. This is of particular advantage when incorporating the viscoelastic properties of CFRP exhibiting nearly linear frequency dependence of the attenuation coefficients [32–34]. Thin interlaminar resin-rich regions are modeled as spring-type interlayer interfaces with equivalent normal and shear stiffnesses [35–41]. The transient reflection waveform from the CFRP laminate immersed in water is obtained by the inverse Fourier transform of the frequency-domain solution. The influence of the content as well as the size of pores on the ultrasonic wave velocity, attenuation coefficient, and interlaminar interface echoes is examined based on the numerical simulations and the corresponding experimental results.

This paper is structured as follows. In Sec. 2, the procedure for the measurement of reflected waves from porosity-containing unidirectional CFRP laminates immersed in water is presented. In Sec. 3, the computational model and the frequency-domain finite element analysis are described. In Sec. 4, the numerical and experimental results of the wave velocity, attenuation coefficient, and interlaminar interface echoes for different contents and size of pores are discussed. The conclusion of this study is summarized in Sec. 5.

2. Experimental procedure

The specimens used in the measurement were unidirectional 24-ply carbon-epoxy composite laminates fabricated using the Toho Tenax UTS50/135 UD prepregs. Besides a porosity-free specimen manufactured under the standard conditions, six other specimens with different levels of porosity were prepared by modifying the compaction scheme and assigning improper curing conditions. The optical micrographs of the cross-section perpendicular to the fibers are shown in Fig. 1 for the representative specimens. The porosity content of each specimen was measured as the area fraction of pores in its micrograph using an image analysis technique, as summarized in Table 1 together with the measured laminate thickness and density. The other dimensions of the specimens were all 100 mm × 120 mm.

The measurement of reflected ultrasonic waves from porosity-containing CFRP

laminates was performed with the pulse-echo technique at normal incidence in water. Two kinds of non-focusing piezoelectric transducers with nominal center frequencies of 2.25 MHz and 10 MHz were used, and the reflection waveforms were digitized with the sampling frequency of 100 MHz. The 2.25 MHz transducer was used for the measurement of the wave velocity and attenuation from the front and back wall echoes. After the Fourier transform was carried out for the recorded waveforms, the wave velocity $V(f)$ and attenuation coefficient $\alpha(f)$ in the thickness direction were obtained as functions of the frequency f using the following equations [42]:

$$V(f)=\frac{4\pi fd}{\theta_{\mathrm{Front}}(f)-\theta_{\mathrm{Back}}(f)+2n\pi}, \tag{1}$$

$$\alpha(f)=\frac{1}{2d}\ln\left[\frac{1-\{R(f)\}^2}{A_{\mathrm{Back}}(f)/A_{\mathrm{Front}}(f)}\right], \tag{2}$$

where $\theta_{\mathrm{Front}}(f)$ ($\theta_{\mathrm{Back}}(f)$) and $A_{\mathrm{Front}}(f)$ ($A_{\mathrm{Back}}(f)$) are the phase and amplitude spectra of the front (back) wall echo, n is an integer to be determined by phase unwrapping, and d is the thickness of the specimen. In Eq. (2), $R(f)$ is the amplitude reflection coefficient at the water-specimen interface given by

$$R(f)=\frac{\rho_{\mathrm{w}}V_{\mathrm{w}}-\rho_{\mathrm{s}}V(f)}{\rho_{\mathrm{w}}V_{\mathrm{w}}+\rho_{\mathrm{s}}V(f)}, \tag{3}$$

where ρ_{w} and V_{w} are the density and the wave speed of water, and ρ_{s} is the density of the specimen. On the other hand, the 10 MHz transducer was used for the characterization of the interlaminar interface echo signals. The time-frequency analysis was then performed by calculating the short-time Fourier transform (STFT) of the reflection waveforms in order to obtain the temporal evolution of the frequency components in the interlaminar interface echoes.

The experimental procedure outlined above was also applied to measure the wave reflection by a polished surface of an aluminum block immersed in water using the same transducers. The recorded reflection waveforms for the two transducers are shown in Fig. 2. These waveforms were regarded to be proportional to those of the incident waves from the transducers, and used as the displacement waveforms of the incident waves in the numerical simulations described below.

3. Two-dimensional frequency-domain finite element analysis

3.1 Computational model

The computational model for the two-dimensional plane-strain ultrasonic wave propagation in a composite laminate is shown in Fig. 3. It occupies the domain of $0 \le x_1 \le L$ and $0 \le x_2 \le 2H_w + H$, and consists of an N-layered unidirectional CFRP laminate of total thickness H ($H_w \le x_2 \le H_w + H$) and water regions of height H_w ($0 \le x_2 \le H_w$ and $H_w + H \le x_2 \le 2H_w + H$). In the present analysis, the length parameters are set as H_w = 1 mm, H = 4.56 mm, N = 24, and L = 10 mm. The computational model in Fig. 3 is discretized by square-shaped four-node isoparametric elements having the identical dimensions of 0.01 mm × 0.01 mm. This element size was chosen to be one-tenth of the minimum wavelength in the analysis, i.e., 0.10 mm at 15 MHz in water.

After the mesh generation is performed for the whole modeled region using 656,000 elements and 680,680 nodes, the elements corresponding to the pores are eliminated. In the micrographs of the cross-sections shown in Fig. 1, pores are observed to be localized at interlaminar interfaces. Therefore, the pores are distributed randomly at the interlaminar interfaces according to the preset content and size in the computational model. As a consequence, individual pores are modeled as cylindrical voids oriented in the x_3 direction with the same square cross-section and size. This is a reasonable approximation within the framework of two-dimensional analysis, since some recent X-ray CT studies [43-45] have revealed that the pores elongated along the fiber direction are dominant in the laminates when the curing conditions are inappropriate. Different porosity contents from 0 % to 7.1 % are modeled in accordance with the specimens used in the measurement. The pore size is modeled in three ways, i.e., 0.05 mm × 0.05 mm, 0.07 mm × 0.07 mm, and 0.10 mm × 0.10 mm. Representative pore distributions for different contents and size are shown in Fig. 4, where the black squares correspond to the pores modeled.

Each ply of the laminate is assumed to contain the fibers aligned parallel to the x_3 direction, and modeled as a homogeneous transversely isotropic viscoelastic medium. In the present frequency-domain analysis, the viscoelastic properties of CFRP are characterized by the complex elastic moduli C_{11} and C_{66} in the Voigt notation. The real and imaginary parts of these moduli are assumed to be independent of the frequency,

corresponding to the linear frequency dependence of the attenuation coefficients commonly observed for CFRP [32–34]. It is noted in passing that incorporating such viscoelastic properties in the direct time-domain analysis requires complicated formulations.

Thin interlaminar resin-rich regions, typically several microns thick, are modeled as spring-type interlayer interfaces with finite normal and shear stiffnesses, K_N and K_T, respectively. The spring boundary conditions [35-41] are applied to the double nodes on the interlaminar interfaces located at $x_2 = H_w + mh$ ($m = 1, 2,\ldots, N - 1$, $h = H/N$: ply thickness). The material properties used in the present analysis are summarized in Table 2. The density and thickness of plies are given in accordance to the porosity-free specimen used in the measurement. The complex elastic constants as well as the interlayer interfacial stiffnesses were determined experimentally for the porosity-free specimen. Namely, they were determined so that the theoretical amplitude transmission coefficients [41] fit best to those measured for the porosity-free specimen at different incident angles in the plane normal to the fiber direction.

As mentioned in Sec. 2, the specimens used in the measurement were manufactured under different curing conditions which resulted in different porosity contents. It is noted, however, that different manufacturing conditions can lead to different states of interlaminar interfaces as well. In the following analysis, this effect is first ignored by using the interfacial stiffnesses determined for the porosity-free specimen in all simulations. Possible effect of varying the interfacial stiffnesses according to the porosity content will be discussed later in Sec. 4.3.

3.2 Frequency-domain finite element analysis

The numerical simulations are run assuming two different center frequencies of the incident wave, i.e., 2.25 MHz and 10 MHz according to the measurements as explained above. Following the formulation by Nakashima *et al*. [46] in the frequency domain, the incidence of the plane longitudinal wave in the positive x_2 direction is simulated, and the reflected and transmitted waves are absorbed at the upper and bottom boundaries, respectively. The amplitude and the phase of the incident wave are given by the Fourier transform of the experimental waveform in Fig. 2 (a) or (b). The periodic boundary

condition is imposed on the left and right boundaries at $x_1 = 0$ and $x_1 = L$. When the time dependence of exp(-$i\omega t$) (t: time) is assumed, the governing system of equations is given as

$$\left(\mathbf{K} - \omega^2 \mathbf{M}\right)\mathbf{u} = \mathbf{F}, \tag{4}$$

where **K** is the global stiffness matrix, **M** is the global mass matrix, **u** is the global nodal displacement vector, and **F** is the global nodal force vector.

The above finite element formulation is implemented in a self-made code written by Fortran 90. Only the non-zero elements of the sparse global matrices are stored using the compressed row storage format [47], and the system of equations (4) is solved by the Intel MKL PARDISO (Parallel Direct Sparse Solver). After solving Eq. (4), the nodal displacements at the upper boundary of the computational model are subtracted by the corresponding incident wave displacements and averaged over the same boundary to obtain the complex reflected wave amplitude. This procedure is repeated for different frequencies (0 to 5 MHz and 0 to 15 MHz in the simulations for the center frequencies of 2.25 MHz and 10 MHz, respectively) with the interval of 0.1 MHz to construct the reflection spectra. After zero-padding to the spectrum for each center frequency up to 50 MHz and making it conjugate-symmetric, the inverse Fourier transform is performed to calculate the transient reflection waveform.

4. Results and discussion

4.1 Velocity and Attenuation

For the incident wave with the center frequency of 2.25 MHz, the computed reflection waveforms are depicted in Fig. 5 together with those measured on the specimens with different porosity contents. The experimental results in Fig. 5 (a) show increasing delay and decreasing amplitude of the back wall echo with increasing porosity content. Figure 5 (b)–(d) show the numerical results for the pore size 0.05 mm × 0.05 mm, 0.07 mm × 0.07 mm, and 0.10 mm × 0.10 mm, respectively. The numerical results also show changes in delay and amplitude depending on the porosity content and the pore size.

Using Eqs. (1)–(3), the wave velocity and attenuation coefficient at the fixed frequency of 2.25 MHz are computed from the numerical reflection waveforms. Their

variations with the porosity content are shown in Fig. 6 for different pore size together with the experimental results. Figure 6 also contains the numerical results when the interlayer interfacial stiffnesses are varied according to the porosity content, which will be discussed later in Sec. 4.3. In Fig. 6, the depicted data points and the vertical error bars express the mean values and the 95 % confidence intervals, respectively, of the observation at 1200 different points on the specimen for the experimental results and of the simulations for 100 different pore arrangements for the numerical results. The horizontal error bars in the experimental results show the maximum and minimum values of the measured porosity contents shown in Table 1. It can be observed that the experimental results for the porosity-free sample are well simulated by the numerical analysis, indicating that the assumed material properties are indeed reasonable.

It is observed in Fig. 6 (a) that the wave velocity obtained from the numerical simulations decreases almost linearly with the porosity content. The slope of the velocity with the porosity content is, however, insensitive to the modeled pore size. The experimental results also exhibit linear variation of the velocity with the porosity content. Its decrease rate is, however, steeper than the numerical results. This quantitative discrepancy indicates that the porosity-containing specimens used in the experiment are different from the porosity-free one not only in the porosity content but also in other properties. Possible effect of variable interlayer interfacial stiffnesses according to the porosity content will be discussed in Sec. 4.3.

In Fig. 6 (b), the simulated attenuation coefficient increases more or less proportionally with the porosity content and shows higher attenuation for larger pore size. The measured attenuation coefficient also increases monotonically with the porosity content. The measured attenuation, however, appears to increase with a higher rate than the proportional increase in the numerical simulations for the fixed pore size. Such behavior has also been reported by Yu *et al.* [31] in their measurement and finite element analysis. In Fig. 6 (b), the porosity-content dependence of the attenuation below 3 % in the experiment is close to the numerical results for the pore size of 0.05 mm. For higher porosity contents, the measured attenuation appears to deviate toward the numerical results for larger pore size, suggesting that the samples of higher porosity content actually have larger pores. This is qualitatively in accord with the micrographic

observation in Fig. 1. In fact, since the higher porosity content is induced by improper curing conditions, it is natural to assume that the pores are more likely to be larger. It is also noted that the top and bottom surfaces of the specimens with higher porosity content tend to have somewhat increased roughness, which can also contribute to the higher attenuation coefficient in the measurement.

4.2 Interlaminar interface echoes

The experimental and simulated reflection waveforms for the incident wave with the center frequency of 10 MHz are compared in Fig. 7 for different porosity contents. In contrast to Fig. 5, persistent ripples can be observed between the front and back wall echoes, which are due to the reflection from the interfaces between the adjacent plies. These echoes are referred to as interlaminar interface echoes here.

Figure 8 illustrates the STFT of experimental and numerical reflection waveforms computed with the Hanning window of time length of 0.6 μs. As shown in Fig. 8 (a) and (b), the interlaminar interface echoes of the porosity-free laminate have a finite bandwidth around 8 MHz. This corresponds to the stop-band frequency mainly governed by the resonance of the longitudinal wave in the stacking direction. As shown in Figs. 7 and 8, their time duration becomes shorter as the porosity content increases or the pore size becomes larger. This can be understood, as higher porosity content or larger pores cause more significant wave scattering to disturb the resonance phenomenon in the layered structure which generates interlaminar interface echoes.

Figure 9 illustrates the cross-sections of the STFT of reflection waveforms at 8 MHz for different porosity contents. The experimental results shown in Fig. 9 represent the averages of the measurement at 1200 different points on the specimen, while the numerical results in Fig. 9 (b) and (c) show the averages of the simulation for 30 different pore arrangements. It can be observed that the 8-MHz components of interlaminar interface echoes decay gradually with time. These spectral amplitudes are fitted by straight lines in the time range between 1.5 and 2 μs using the least square method. In Fig. 10, the calculated slopes (temporal decay rates) are shown against the porosity content. Clearly, the decay rate becomes steeper as the porosity content increases. It is also seen that the numerical results are not very sensitive to the pore size.

The experimental results have some scatters but show similar dependence on the porosity content.

In previous works, the interlaminar interface echoes were characterized in different ways for porosity characterization. Grolemund and Tsai [29] showed that the ensemble mean of the echo signals is correlated well with the porosity content. Dominguez *et al*. [28] used the temporal change of the energy of these signals to differentiate the localized porosity. Kim *et al*. [30] demonstrated that certain wavelet coefficients of the backscattered echoes can be correlated well with the porosity content. It is noted that the change in the temporal decay rate of the spectral amplitude at the stop-band frequency discussed here is a direct measure of the perturbation of the interlayer resonance by the porosity. The present results indicate that it is potentially a good measure of the porosity content in the composite laminate.

4.3. Effect of variable interlayer interfacial stiffness

The numerical results discussed above are obtained using the interlayer interfacial stiffnesses determined for the porosity-free specimen. As a result, there is some quantitative discrepancy between the measured and the simulated porosity-content dependence of the wave velocity as shown in Fig. 6 (a), while the measured attenuation as well as the interlaminar interface echo characteristics are reasonably reproduced by the numerical simulations as shown in Fig. 6 (b) and Fig. 10.

If the interlaminar resin-rich regions are considered as a homogeneous resin layer of equivalent thickness h_e, the interlayer interfacial stiffnesses can be simply estimated by [36]

$$K_N = \frac{\lambda_e + 2\mu_e}{h_e}, \qquad K_T = \frac{\mu_e}{h_e}, \tag{5}$$

where λ_e and μ_e are Lamé's constants of resin. These relations indicate that the decrease of resin moduli or the increase of resin layer thickness gives lower interfacial stiffnesses. In Fig. 11 showing the enlarged cross-sections of the specimens, it is seen that the interlaminar resin-rich regions are thicker when the porosity content is higher. This feature is also in line with the observation of Yu *et al*. [31] for quasi-isotropic CFRP

laminates. Therefore, it is reasonable to assume that the specimens with higher porosity contents are associated with lower interlayer interfacial stiffnesses.

Motivated by the above reasoning, the following relations between the stiffnesses and the porosity content are tested in numerical simulations.

$$K_{\mathrm{N}} = \frac{K_{\mathrm{N0}}}{1+ap}, \quad K_{\mathrm{T}} = \frac{K_{\mathrm{T0}}}{1+ap}. \tag{6}$$

In these expressions, K_{N0} and K_{T0} are the interfacial stiffnesses of the porosity-free laminate given in Table 2, p is the porosity content ($0 < p < 1$), and a is a non-dimensional constant. The best fit of the numerical results for the pore size of 0.05 mm × 0.05 mm to those measured regarding the porosity-content dependence of the wave velocity gives $a = 56.3$. This result implies that the increase in porosity content to 7 % reduces the interfacial stiffnesses down to about one fifth of those of the porosity-free sample. The thickness change alone does not explain this amount of change if Eq. (5) is assumed literally. It should be noted, however, that in the presence of porosity the interlaminar regions cannot be simply regarded as a thin resin layer of uniform thickness. It is also likely that the resin viscoelastic properties can also be affected to some degree by insufficient curing conditions.

When the pore size is fixed to 0.05 mm × 0.05 mm and the interlayer interfacial stiffnesses are varied according to Eq. (6) with the tuned parameter $a = 56.3$, the wave velocity, attenuation coefficient, and temporal decay rate of interlaminar interface echoes are shown in Fig. 6 (a), (b), and Fig. 10, respectively. In Fig. 6 (a), the variation of wave velocity with the porosity content is now favorably compared with the experimental results. In Fig. 6 (b), the attenuation coefficient for the variable interfacial stiffnesses hardly changes from the results for the fixed stiffnesses. Similarly, in Fig. 10 the temporal decay rate of interlaminar interface echoes is affected only slightly by varying the interfacial stiffnesses, and remains to be in reasonable agreement with the experiment.

5. Conclusion

In the present study, the two-dimensional finite element analysis of the ultrasonic wave propagation in porosity-containing unidirectional CFRP laminates has been

carried out by modeling different pore contents and size. The linearly frequency-dependent attenuation of the porosity-free CFRP and the presence of interlaminar resin-rich regions have been incorporated in the frequency-domain analysis. The transient reflection waveforms have been calculated using the inverse Fourier transform. From the simulated reflection waveforms, the ultrasonic wave velocity, attenuation coefficient, and the decay rate of the interlaminar interface echoes have been obtained. The influence of porosity content and pore size on these ultrasonic parameters has been discussed based on the numerical as well as experimental results.

As a result, it has been found that the wave velocity and attenuation vary monotonically with the porosity content. The relation between the attenuation and the porosity content also depends on the pore size. The temporal decay rate of the interlaminar interface echoes at the stop-band frequency is correlated well with the porosity content in a manner relatively insensitive to the pore size. By adjusting the interlayer interfacial stiffnesses according to the porosity content, the agreement between the measured and computed wave velocity has been improved, indicating that improper manufacturing conditions vary not only the porosity content but also the interlaminar interfacial properties. This finding suggests that proper modeling of interlaminar interfaces is important for analyzing the ultrasonic wave propagation in composite laminates.

It is also noted that the present two-dimensional numerical simulations assumed relatively simple geometries of the distributed pores, namely, cylindrical voids all aligned in the out-of-plane direction. While this is a justifiable approximation for unidirectional laminates, the pore morphology for other lay-ups such as cross-ply laminates needs three-dimensional modeling. Such modeling and simulations are left for future investigations.

Acknowledgement

This work has been partly supported by JSPS KAKENHI Grant Numbers 25-1754 and 15K13833. The authors are grateful to Mr. M. Ohno, Kawaju Gifu Engineering Co., Ltd., for his contribution in fabricating the specimens used in the present study.

References

[1] R. A. Smith. Composite defects and their detection. Mater Sci Eng 2009; III: 103–143.

[2] E. Birt, R. A. Smith. A review of NDE methods for porosity measurement in fibre-reinforced polymer composites. Insight 2004; 46: 681–686.

[3] K. J. Bowles, S. Frimpong. Void effects on the interlaminar shear strength of unidirectional graphite-fiber-reinforced composites. J Compos Mater 1992; 26: 1487–1509.

[4] P. Olivier, J. P. Cottu, B. Ferret. Effects of cure cycle pressure and voids on some mechanical properties of carbon/epoxy laminates. Composites 1995; 26: 509–515.

[5] H. Jeong. Effects of voids on the mechanical strength and ultrasonic attenuation of laminated composites. J Compos Mater 1997; 31: 276–292.

[6] M. L. Costa, S. F. M. Almeida, M. C. Rezende. The influence of porosity on the interlaminar shear strength of carbon/epoxy and carbon/bismaleimide fabric laminates. Compos Sci Tech 2001; 61: 2101–2108.

[7] P. A. Olivier, B. Mascaro, P. Margueres, F. Collombet. CFRP with voids: ultrasonic characterization of localized porosity, acceptance criteria and mechanical characteristics. Proceedings of the 16th International Conference on Composite Materials 2007.

[8] S. F. M. Almeida, Z. S. N. Neto. Effects of void content on the strength of composite laminates. Compos Struct 1994; 28: 139–148.

[9] J. -M. Tang, W. I. Lee, G. S. Springer. Effects of cure pressure on resin flow, voids, and mechanical properties. J Compos Mater 1987; 21: 421–440.

[10] B. G. Martin. Ultrasonic wave propagation in fiberreinforced solids containing voids. J Appl Phys 1977; 48: 3368–3373.

[11] W. N. Reynolds, S. J. Wilkinson. The analysis of fibre-reinforced porous composite materials by the measurement of ultrasonic wave velocities. Ultrasonics 1978; 16: 159–163.

[12] D. K. Hsu, H. Jeong. Ultrasonic velocity change and dispersion due to porosity in composite laminates. Rev Prog Quant Nondest Eval 1989; 8B: 1567–1573.

[13] I. N. Komsly, I. M. Daniel, S. C. Wooh. Characterization of porosity in thick composites using ultrasonic wave velocity measurements. Rev Prog Quant Nondest Eval 1993; 12A: 1273–1280.

[14]H. Jeong, D. K. Hsu. Experimental analysis of porosity-induced ultrasonic attenuation and velocity change in carbon composites. Ultrasonics 1995; 33: 195–203.

[15]J. Ito, S. Biwa, T. Hayashi, A. Kuraishi. Ultrasonic wave propagation in the corner section of composite laminate structure: Numerical simulations and experiments. Compos Struct 2015; 123: 78–87.

[16]D. E. W. Stone, B. Clarke. Ultrasonic attenuation as a measure of void content in carbon-fibre reinforced plastics. Non-destructive Testing 1975; 137-145.

[17]B. G. Martin. Ultrasonic attenuation due to voids in fibre-reinforced plastics. NDT Int 1976; 9: 242–246.

[18]D. K. Hsu, S. M. Nair. Evaluation of porosity in graphite-epoxy composite by frequency dependence of ultrasonic attenuation. Rev Prog Quant Nondest Eval 1987; 6A: 1185–1193.

[19]J. M. Hale, J. N. Ashton. Ultrasonic attenuation in voided fibre-reinforced plastics. NDT Int 1988; 21: 321–326.

[20]J. G. Miller. Quantitative non-destructive evaluation of porous composite materials based on ultrasonic wave propagation. Topical Semiannual Progress Report 1988; 1-28, NASA-CR-182544.

[21]S. M. Nair, D. K. Hsu, J. H. Rose. Porosity estimation using the frequency dependence of the ultrasonic attenuation. J Nondestruct Eval 1989; 8: 13–26.

[22]I. M. Daniel, S. C. Wooh, I. Komsky. Quantitative porosity characterization of composite materials by means of ultrasonic attenuation. J Nondestruct Eval 1992; 11: 1–8.

[23]F. A. Reed, T. J. Batzinger, R. W. Reed. Porosity measurement in composites using ultrasonic attenuation methods. Rev Prog Quant Nondest Eval 1993; 12: 1265–1272.

[24]J. E. Michaels, T. E. Michaels, S. Jönsson. Ultrasonic methods for detection of micro porosity in composite materials. Rev Prog Quant Nondest Eval 1993; 12: 1281–1287.

[25]L. Lin, M. Luo, H. T. Tian, X. M. Li, G. P. Guo. Experimental investigation on porosity of carbon fiber-reinforced composite using ultrasonic attenuation coefficient. Proceedings of the 17th World Conference on Nondestructive Testing 2008.

[26]L. Lin, X. Zhang, J. Chen, Y. Mu, X. Li. A novel random void model and its application in predicting void content of composites based on ultrasonic attenuation coefficient.

Appl. Phys. A 2011; 103: 1153–1157.

[27]L. Lin, J. Chen, X. Zhang, X. Li. A novel 2-D random void model and its application in ultrasonically determined void content for composite materials. NDT&E Int 2011; 44: 254–260.

[28]N. Dominguez, B. Mascaro. Ultrasonic non-destructive inspection of localized porosity in composite materials. Proceedings of the 9th European Conference on Non-Destructive Testing 2006; Tu.2.1.4.

[29]D. Grolemund, C. Tsai. Statistical moments of backscattered ultrasound in porous fiber reinforced composites. IEEE Trans Ultrason Ferroelectr Freq Control 1998; 45: 295–304.

[30]K. B. Kim, D. K. Hsu, D. J. Barnard. Estimation of porosity content of composite materials by applying discrete wavelet transform to ultrasonic backscattered signal. NDT&E Int 2013; 56: 10–16.

[31]Y. Yu, J. Ye, Y. Wang, B. Zhang, G. Qi. A mesoscale ultrasonic attenuation finite element model of composites with random-distributed voids. Compos Sci Tech 2013; 89: 44–51.

[32]W. N. Reynolds, L. P. Scudder, H. Pressman. The use of ultrasonic wave attenuation to monitor polymer and composite quality. Polymer Testing 1986; 6: 325–336.

[33]T. D. Lhermitte, S. M. Handley, M. R. Holland, J. G. Miller. Anisotropy of the frequency-dependent ultrasonic attenuation in unidirectional graphite/epoxy composite material. Proceedings of the IEEE Ultrasonic Symposium 1991; 819–823.

[34]S. Biwa, Y. Watanabe, N. Ohno. Analysis of wave attenuation in unidirectional viscoelastic composites by a differential scheme. Compos Sci Tech 2003; 63: 237-247.

[35]J.-M. Baik, R. B. Thompson. Ultrasonic scattering from imperfect interfaces: a quasi-static model. J Nondestruct Eval 1985; 4: 177–196.

[36]S. I. Rokhlin, Y. J. Wang. Analysis of boundary conditions for elastic wave interaction with an interface between two solids. J Acoust Soc Am 1991; 89: 503–515.

[37]S. I. Rokhlin, W. Huang. Ultrasonic wave interaction with a thin anisotropic layer between two anisotropic solids: Exact and asymptotic-boundary-condition methods. J Acoust Soc Am 1992; 92: 1729–1742.

[38]P. Fraisse, F. Schmit, A. Zarembowitch. Ultrasonic inspection of very thin adhesive

layers. J Appl Phys 1992; 72: 3264–3271.

[39] Y. Ishii, S. Biwa. Ultrasonic evaluation of interlayer interfacial stiffness of multilayered structures. J Appl Phys 2012; 111: 084907.

[40]Y. Ishii, S. Biwa. Evaluation of interlayer interfacial stiffness and layer wave velocity of multilayered structures by ultrasonic spectroscopy. J Acoust Soc Am 2014; 136: 183–191.

[41]Y. Ishii, S. Biwa. Transmission of ultrasonic waves at oblique incidence to composite laminates with spring-type interfaces. J Acoust Soc Am 2015; 138: 2800-2810.

[42]R. A. Kline, D. M. Egle. Applications of digital methods to ultrasonic materials characterization. NDT Int 1986; 19: 341–347.

[43]S. Hernández, F. Sket, J. M. Molina-Aldareguía, C. González, J. LLorca. Effect of curing cycle on void distribution and interlaminar shear strength in polymer-matrix composites, Compos Sci Tech 2011; 71: 1331-1341.

[44]J. E. Little, X. Yuan, M. I. Jones. Characterisation of voids in fibre reinforced composite materials. NDT & E Int 2012; 46: 122-127.

[45]S. Hernández, F. Sket, C. González, J. LLorca. Optimization of curing cycle in carbon fiber-reinforced laminates: Void distribution and mechanical properties. Compos Sci Tech 2013; 85: 73-82.

[46]K. Nakashima, S. Biwa, E. Matsumoto. Elastic wave transmission and stop band characteristics in unidirectional composites. J Solid Mech Mater Eng 2008; 2: 1195–1206.

[47]R. Barrett, M. Berry, T. F. Chan, J. Demmel, J. M. Donato, J. Dongarra, V. Eijkhout, R. Pozo, C. Romine, H. V. D. Vorst. Templates for the solution of linear systems: building blocks for iterative methods. Soc Indust Appl Math 1994; 57–60.

Table 1

Porosity content, thickness, and density of the 24-ply unidirectional CFRP laminate specimens.

Sample number	1	2	3	4	5	6	7
Porosity content [%]	0.0	1.0 ± 0.4	2.1 ± 0.6	2.7 ± 0.3	3.1 ± 0.3	4.6 ± 0.2	7.1 ± 0.4
Thickness [mm]	4.54	4.58	4.60	4.60	4.64	4.74	4.80
Density [$\times 10^3$ kg/m^3]	1.54	1.53	1.52	1.52	1.51	1.48	1.46

Table 2

Material properties assumed in the finite element analysis.

Number of plies N		24
Density of ply ρ [$\times 10^3$ kg/m^3]		1.54
Thickness of ply h [mm]		0.19
Complex elastic constants of ply [GPa]	C_{11}	$3.3 - 0.13\,i$
(transverse isotropy with x_3 as fiber direction)	C_{66}	$13.9 - 0.29\,i$
Interlayer interfacial stiffnesses [GPa/μm]	K_N	2.4
	K_T	0.8
Density of water ρ_w [$\times 10^3$ kg/m^3]		1.00
Wave speed in water V_w [km/s]		1.50

Figure captions

Fig. 1 Micrograph of cross-sections perpendicular to the fiber direction of 24-ply unidirectional CFRP laminate specimens with different porosity contents.

Fig. 2 Reflection waveforms for a polished surface of an aluminum block by (a) the 2.25 MHz transducer, and by (b) the 10 MHz transducer.

Fig. 3 Finite element model for a unidirectional CFRP laminate immersed in water.

Fig. 4 Distributions of pores with different contents and size.

Fig. 5 (a) Experimental and (b)-(d) numerical reflection waveforms of the porosity-containing unidirectional CFRP laminates for the nominal frequency of 2.25 MHz.

Fig. 6 Variation of (a) wave velocity and (b) attenuation coefficient with porosity content at 2.25 MHz.

Fig. 7 (a) Experimental and (b)-(d) numerical reflection waveforms of the porosity-containing unidirectional CFRP laminates for the nominal frequency of 10 MHz.

Fig. 8 Short-time Fourier transform of experimental and numerical reflection waveforms for different porosity contents.

Fig. 9 Cross-sections of the short time Fourier transform at 8 MHz for porosity contents (a) 0.0 %, (b) 2.1 %, and (c) 7.1 %.

Fig. 10 Variation of temporal decay rate of interlaminar interface echoes at 8 MHz with porosity content.

Fig. 11 Magnification of cross-sections of CFRP laminate specimens in Fig. 1.

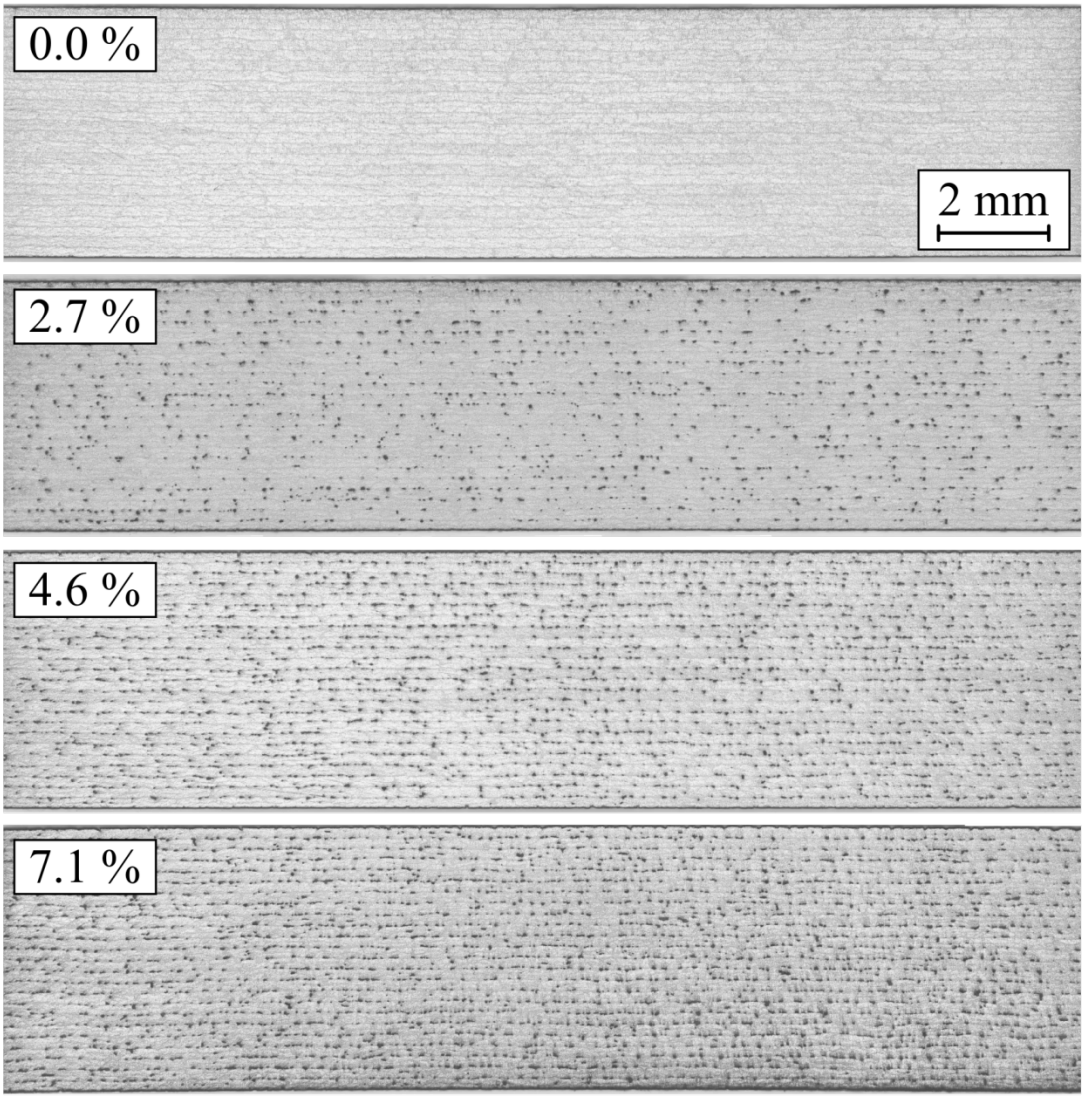

Fig. 1

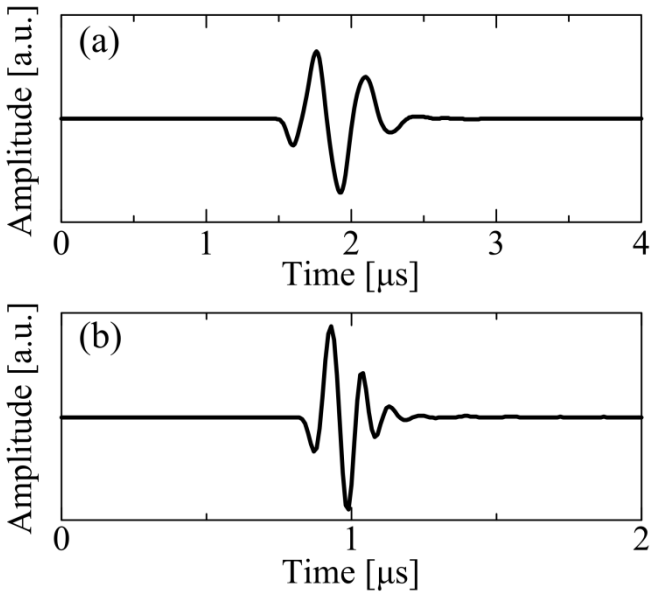
(a)
Amplitude [a.u.]
0
1
2
3
4
Time [μs]
(b)
Amplitude [a.u.]
0
1
2
Time [μs]

Fig. 2

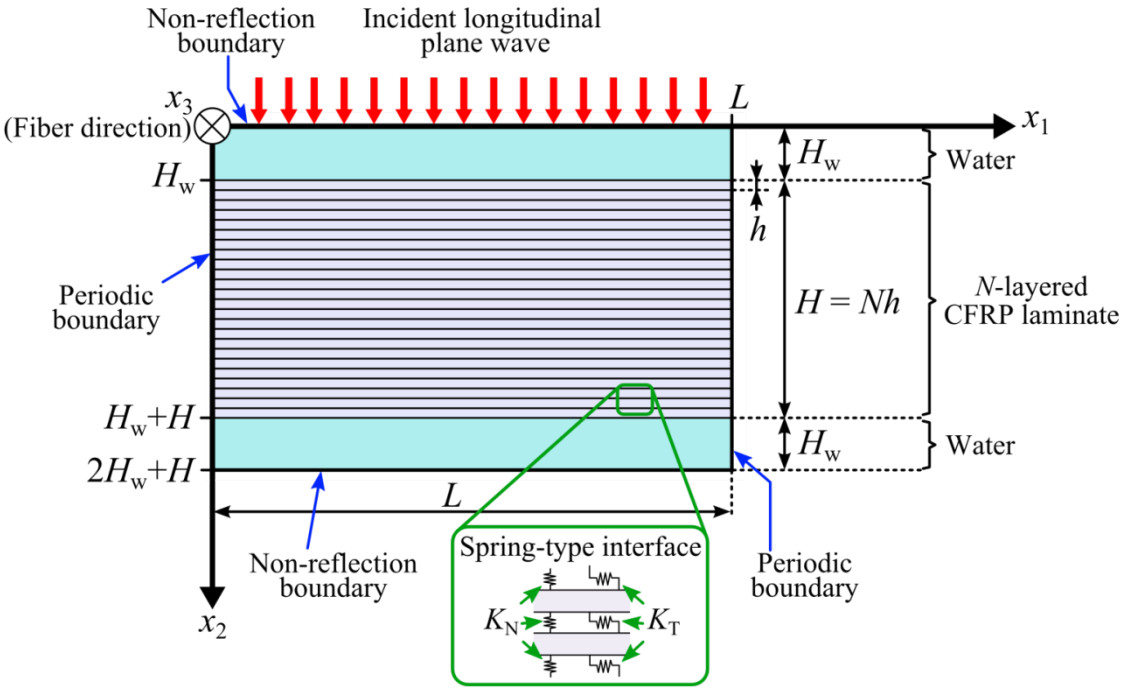
Non-reflection boundary
Incident longitudinal plane wave
x_3
(Fiber direction)
L
x_1
H_w
H_w
Water
h
Periodic boundary
$H = Nh$
N-layered CFRP laminate
H_w+H
H_w
Water
$2H_w+H$
L
Non-reflection boundary
Spring-type interface
K_N
K_T
Periodic boundary
x_2

Fig. 3

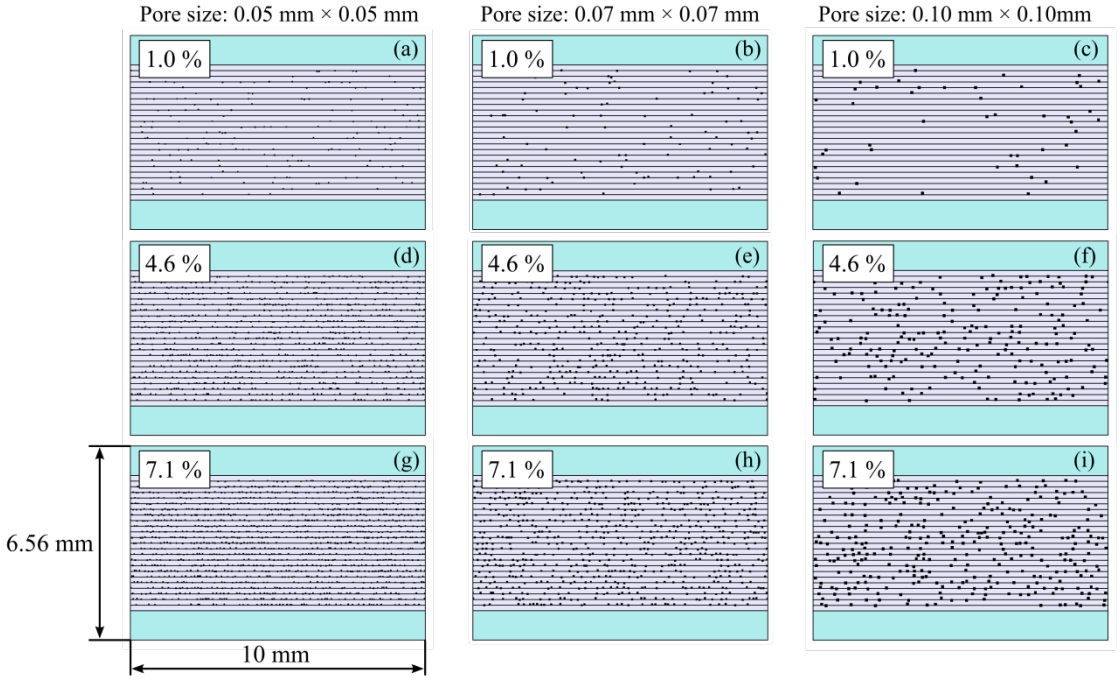
Pore size: 0.05 mm × 0.05 mm
Pore size: 0.07 mm × 0.07 mm
Pore size: 0.10 mm × 0.10mm
1.0 %
(a)
1.0 %
(b)
1.0 %
(c)
4.6 %
(d)
4.6 %
(e)
4.6 %
(f)
7.1 %
(g)
7.1 %
(h)
7.1 %
(i)
6.56 mm
10 mm

Fig. 4

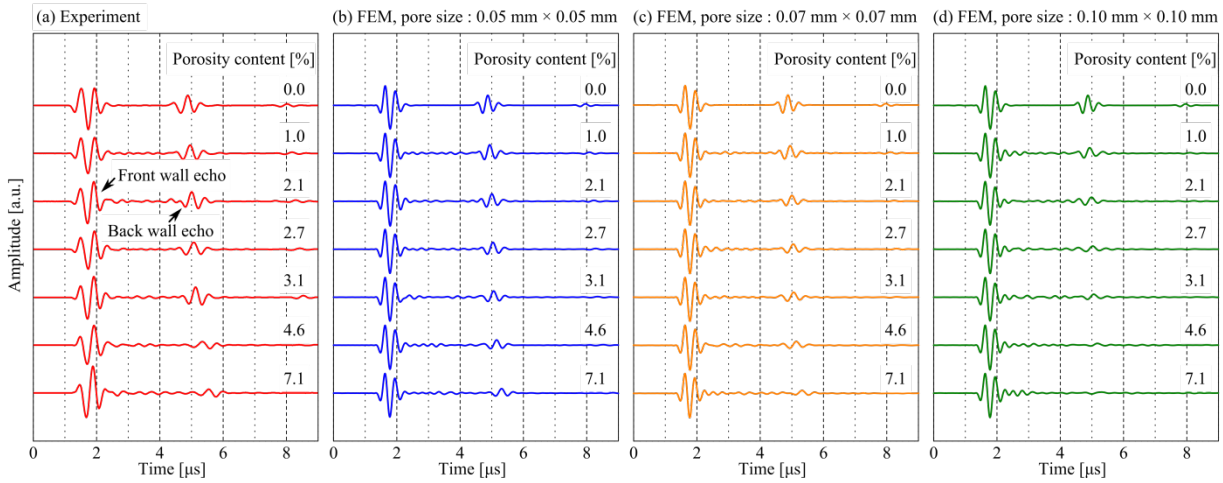
(a) Experiment
(b) FEM, pore size : 0.05 mm × 0.05 mm
(c) FEM, pore size : 0.07 mm × 0.07 mm
(d) FEM, pore size : 0.10 mm × 0.10 mm
Porosity content [%]
0.0
1.0
2.1
2.7
3.1
4.6
7.1
Front wall echo
Back wall echo
Amplitude [a.u.]
Time [μs]
0
2
4
6
8

Fig. 5

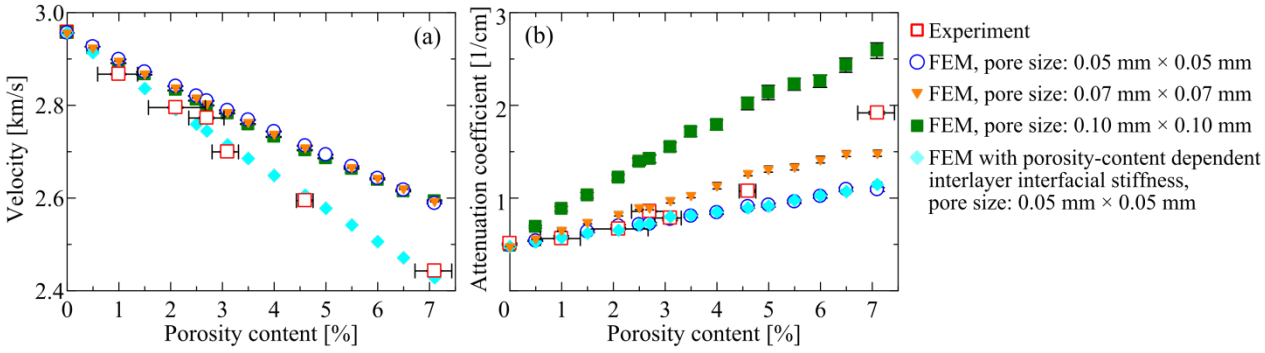
(a)
(b)
Velocity [km/s]
Attenuation coefficient [1/cm]
Porosity content [%]
Porosity content [%]
Experiment
FEM, pore size: 0.05 mm × 0.05 mm
FEM, pore size: 0.07 mm × 0.07 mm
FEM, pore size: 0.10 mm × 0.10 mm
FEM with porosity-content dependent interlayer interfacial stiffness, pore size: 0.05 mm × 0.05 mm

Fig. 6

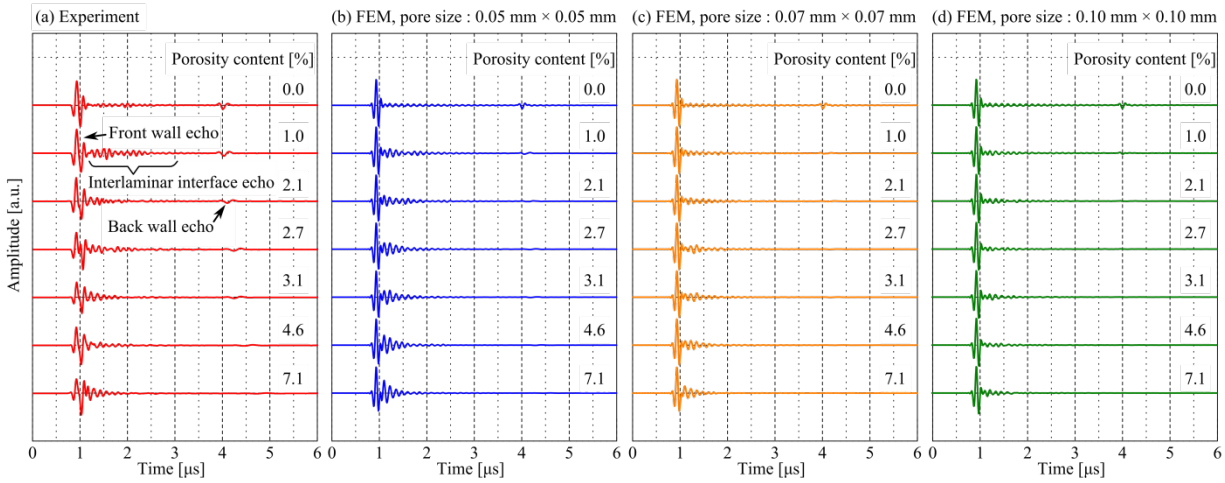
(a) Experiment
(b) FEM, pore size : 0.05 mm × 0.05 mm
(c) FEM, pore size : 0.07 mm × 0.07 mm
(d) FEM, pore size : 0.10 mm × 0.10 mm
Porosity content [%]
0.0
1.0
2.1
2.7
3.1
4.6
7.1
Front wall echo
Interlaminar interface echo
Back wall echo
Amplitude [a.u.]
Time [μs]

Fig. 7

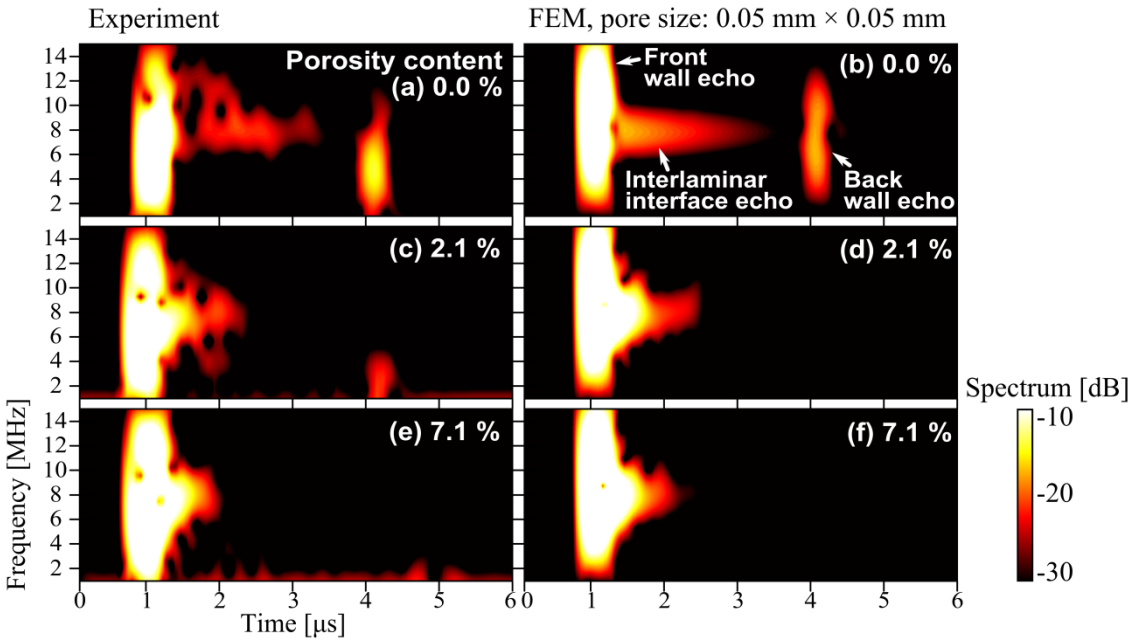
Experiment
FEM, pore size: 0.05 mm × 0.05 mm
Porosity content
(a) 0.0 %
Front wall echo
(b) 0.0 %
Interlaminar interface echo
Back wall echo
(c) 2.1 %
(d) 2.1 %
(e) 7.1 %
(f) 7.1 %
Frequency [MHz]
Time [μs]
Spectrum [dB]
-10
-20
-30

Fig. 8

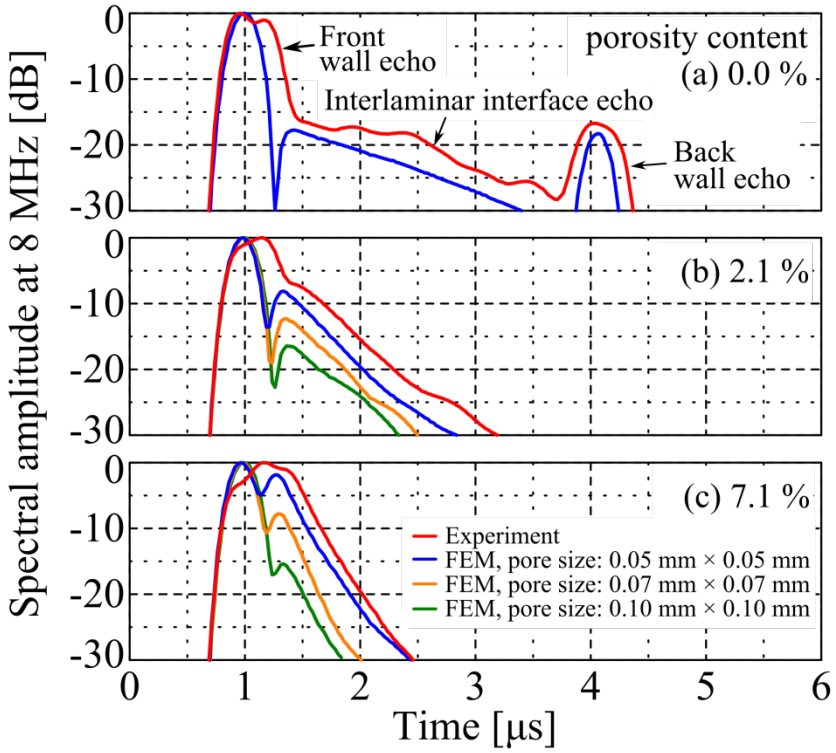
Front wall echo
porosity content
(a) 0.0 %
Interlaminar interface echo
Back wall echo
(b) 2.1 %
(c) 7.1 %
Experiment
FEM, pore size: 0.05 mm × 0.05 mm
FEM, pore size: 0.07 mm × 0.07 mm
FEM, pore size: 0.10 mm × 0.10 mm
Spectral amplitude at 8 MHz [dB]
Time [μs]

Fig. 9

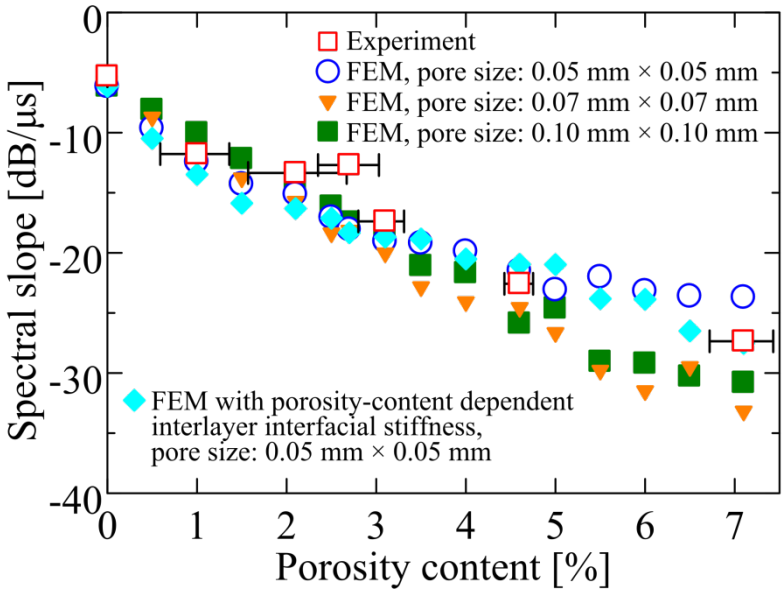
Experiment
FEM, pore size: 0.05 mm × 0.05 mm
FEM, pore size: 0.07 mm × 0.07 mm
FEM, pore size: 0.10 mm × 0.10 mm
FEM with porosity-content dependent interlayer interfacial stiffness, pore size: 0.05 mm × 0.05 mm
Spectral slope [dB/μs]
Porosity content [%]
0
-10
-20
-30
-40
0
1
2
3
4
5
6
7

Fig. 10

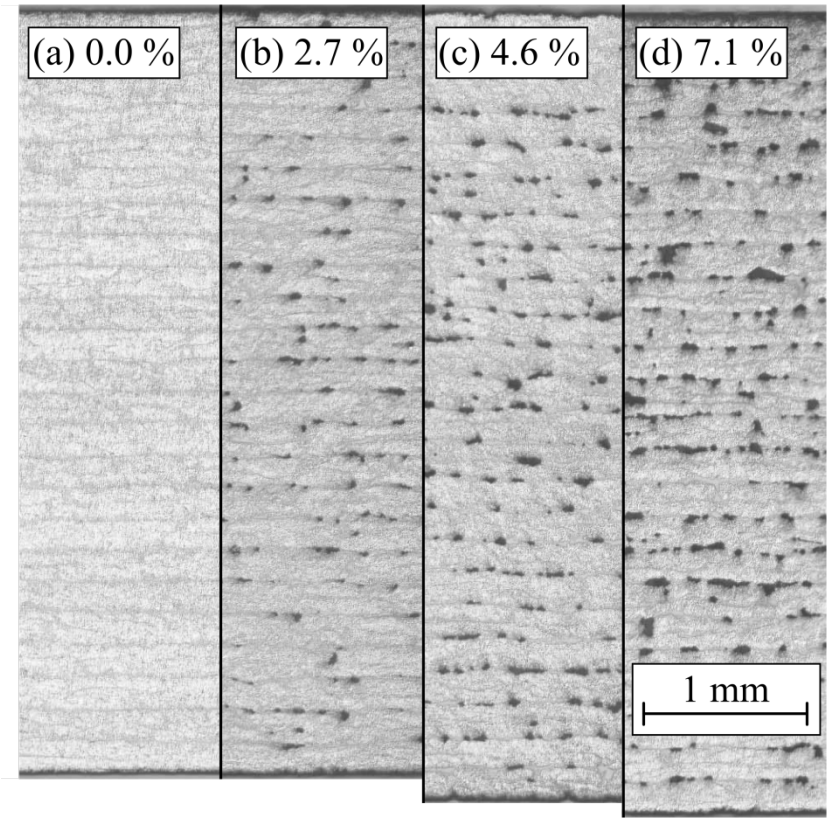
(a) 0.0 %
(b) 2.7 %
(c) 4.6 %
(d) 7.1 %
1 mm

Fig. 11